Supplementary Information for:

Liquid metal universal grippers for ultra-gentle, highly-adaptable, multiscale, and fast manipulations

Xuanhan Chen[1]†, Mingkui Zhang[1]†, Lu Cao[2]†, Long Wang[1], Yue Chen[1], Hao Lin[1], Mingyuan Sun[3], Shiyuan Tong[3], Yuguo Deng[4], Weihua Li[5], Lining Sun[1], Shiwu Zhang[3]*, Shi-Yang Tang[6,7]*, Xiangpeng Li[1]*

[1]College of Mechanical and Electrical Engineering, Soochow University, Suzhou, 215000, China

[2]College of Engineering, Peking University, Beijing, 100871, China

[3]CAS Key Laboratory of Mechanical Behavior and Design of Materials, Department of Precision Machinery and Precision Instrumentation, University of Science and Technology of China, Hefei, 230026, China

[4]State Key Laboratory of Robotics and Systems, Harbin Institute of Technology, Harbin, 150001, China

[5]School of Mechanical Materials Mechatronic and Biomedical Engineering, University of Wollongong, Wollongong, NSW, 2522, Australia

[6]School of Mechanical and Manufacturing Engineering, The University of New South Wales, Sydney, NSW 2052, Australia

[7]School of Electronics and Computer Science, University of Southampton, SO17 1BJ, UK

†These authors contributed equally: Xuanhan Chen, Mingkui Zhang, Lu Cao

*Corresponding authors.

*E-mail: licool@suda.edu.cn; swzhang@ustc.edu.cn; shiyang.tang2@unsw.edu.au

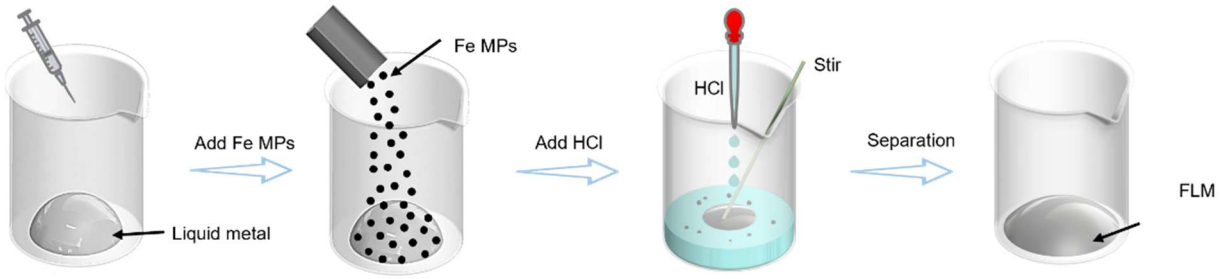

Supplementary Figure 1. Fabrication process for functional liquid metal.

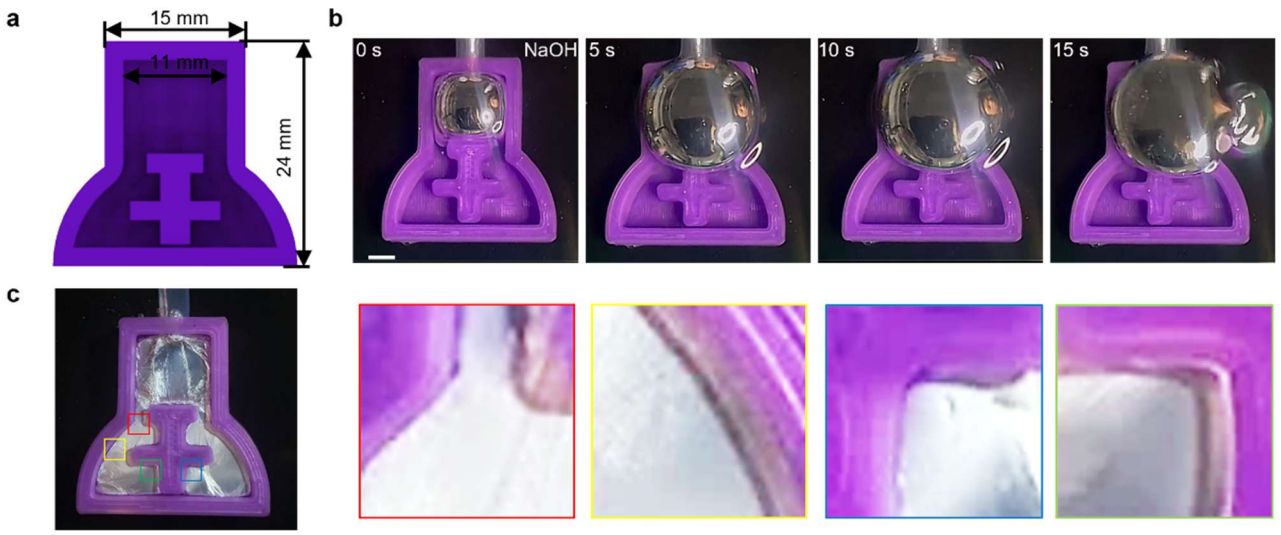

Supplementary Figure 2. Wrapping performance of the FLM. (a) Schematic showing the 3D-printed top-opened mold. (b) Injection of FLM when without the application of an oxidative potential. Scale bar: 5 mm. (c) Wrapping of complex structure using the FLM upon the application of an oxidative potential, all structural features of the mold chamber are tightly enveloped.

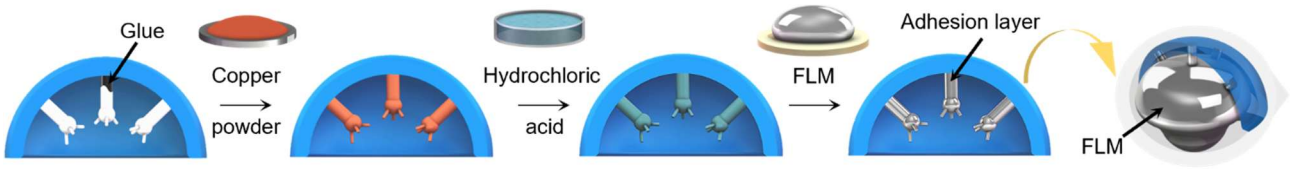

Supplementary Figure 3. Fabrication process of micropillars.

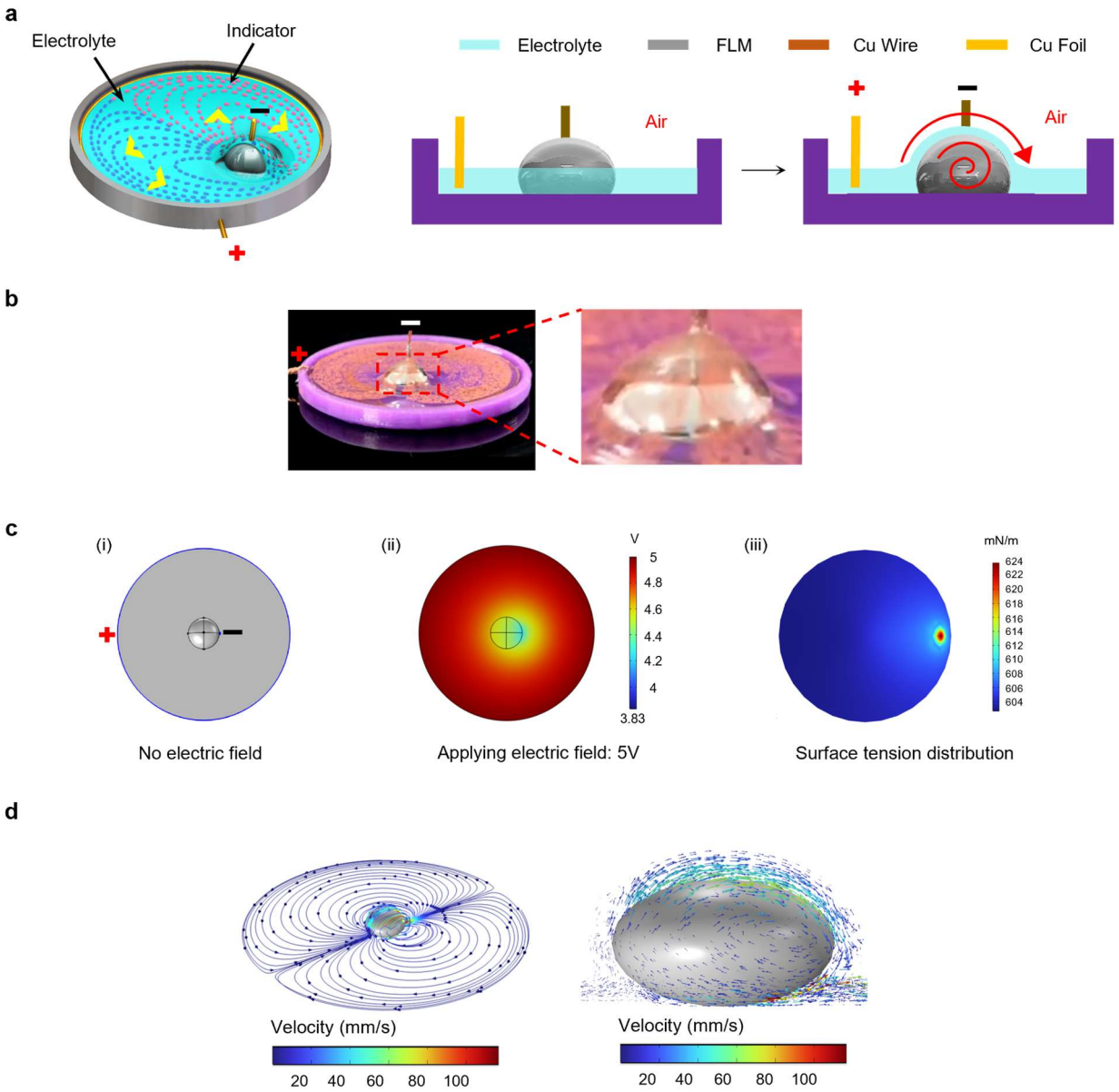

Supplementary Figure 4. (a) Experiment setup of surface tension control system. (b) Actual image showing the fluid flow induced by the Marangoni effect. (c) COMSOL simulation for the surface electric field and surface tension distributions of an FLM droplet. (d) Simulation results for the induced Marangoni flows.

In non-electrolyte environments like the air, only the top hemisphere of the FLM droplet in the gripper cavity contacts the electrolyte in the gauze. The bottom hemisphere of the FLM droplet is exposed to

air. However, the LiMU gripper is still applicable in non-electrolyte environments with the aid of the surface tension control system, which induced the formation of Marangoni flows that allow the electrolyte to move to the region exposed to air. We illustrated the effect caused by Marangoni flows using an FLM droplet with half of it immersed in NaOH solution and the other exposed to the air, as shown in **Supplementary Fig. 3a**. The induced Marangoni effect enables the electrolyte to wrap the exposed surface of the FLM in a very short time, thus maintaining the electrical activity of the whole FLM droplet (**Supplementary Fig. 3b**).

An FLM droplet (volume of 130 μL, diameter of 6 mm) was restricted in a rounded groove located in the center of a 3D-printed circular container (diameter of 5 cm, PLA, 3D printed by HORI printer). NaOH solution (0.5 M) was filled in the container with a depth of 0.5 mm. A circular copper wire (diameter of 0.8 mm) was twined around the internal wall of the container, and another copper wire was inserted into the FLM droplet. The two copper wires were connected to the DC power supply (IT6432, ITECH, China) as electrodes. Copper powder (diameter of 300 nm) was sprinkled into the NaOH solution as an indicator. When applying a negative voltage to the FLM droplet, we observed that the electrolyte flows towards the FLM droplet along a specific radial direction, passing the top hemisphere of the droplet, and sequentially flowing back along the circumferential direction. Interestingly, we first observed that two independent vortices were formed symmetrically along the radial direction, as shown in **Supplementary Video 4**. When moving the electrode to shift the FLM droplet away from the center, the flow direction always keeps along the radial direction towards the center of the circular container. We demonstrated that the hydrodynamic behavior is attributed to the electrically induced Marangoni effect of the FLM (see “COMSOL simulation for surface activity mechanism of the FLM” in Methods).

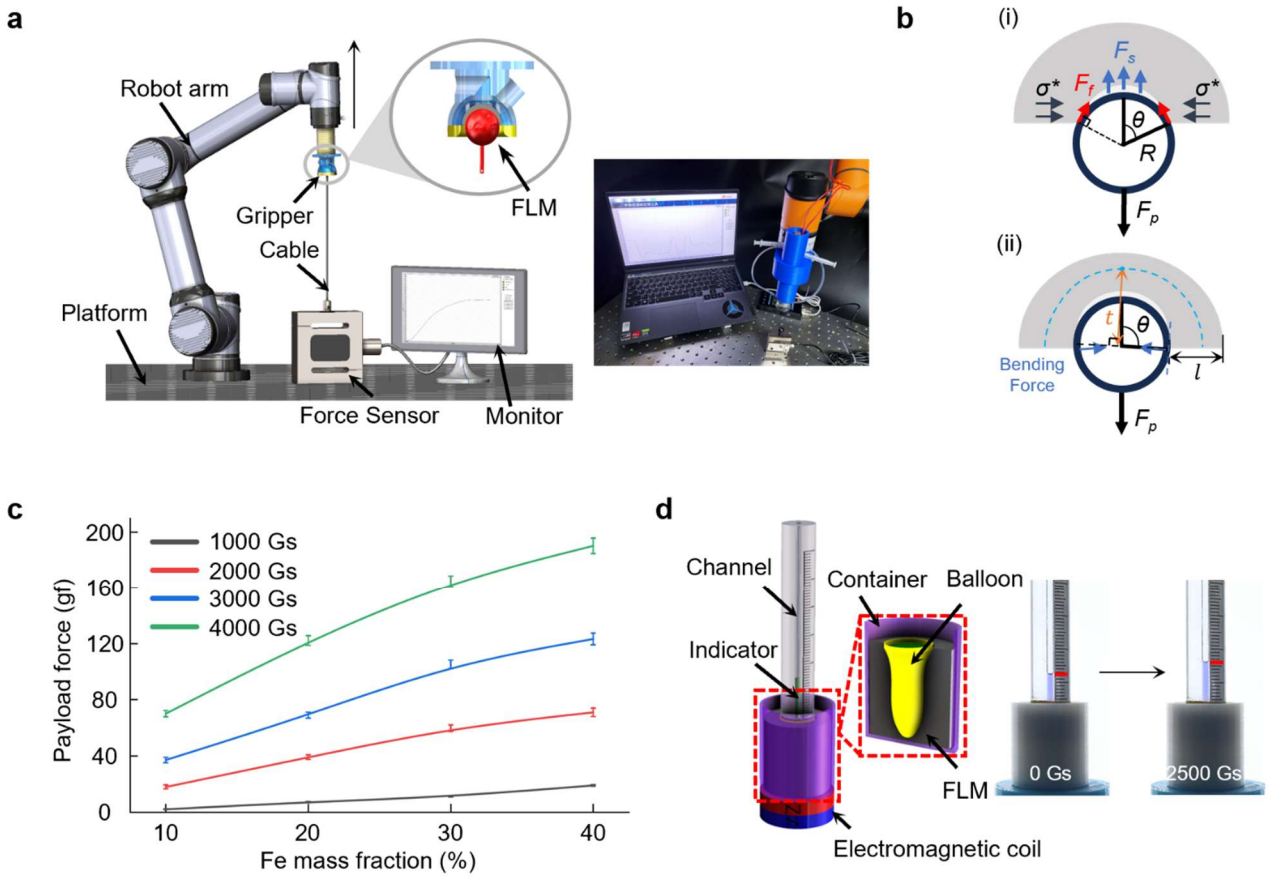

Supplementary Figure 5. (a) The robotic testing system to characterize the payload capacity of the LiMU gripper. (b) Grasping modeling of the LiMU gripper with the ball-and-socket joint. (c) Plots of payload force vs Fe content under different applied magnetic field intensities. (d) Setup of the contact pressure measurement system for measuring the contact pressure exerted by the LiMU gripper.

We developed a robotic testing system to quantitatively characterize the payload capacity of the LiMU gripper, as shown in **Supplementary Fig. 5a**. The LiMU gripper was mounted to a 6-DOF robotic arm (AUBO-i5, AUBO Robotics Technology Co., LTD). The inner diameter of the gripper cavity is 26 mm, and the volume of the injected FLM droplet is 2.5 mL. A DC power supply (IT6432, ITECH, China) was used to drive the electromagnetic coil. For comparability, a 3D-printed sphere hook (diameter of 10 mm) was pre-immersed in the FLM with a certain embedding angle and connected to a force sensor (LY-103, Bengbu Ocean Sensing System Engineering Co., LTD) with a cotton rope. During the

experiment, the robot arm was controlled to move far away from the force sensor along the axial direction of the force sensor. The real-time force-displacement data was recorded by a computer. The maximum payload force can be obtained by analyzing the yield point of the force-displacement curve.

The FLM under the magnetorheological effect can be treated as an elastic medium. Thus, the FLM-wrapped sphere pairs can be analogous to the differential thermal contraction in a ball-and-socket joint[12]. The LiMU gripper pinches the sphere around the gripper-sphere contact line, with a pinching stress σ^* applied on the thin band of width centered at the embedding angle θ (**Supplementary Fig. 5b (i)**). The payload capacity of the LiMU gripper can be estimated similarly to the tensile strength of the ball-and-socket joint, which varies with its embedded angle θ.

The payload force characterization under different embedded angles (sphere diameter: 10 mm, magnetic field intensity: 3000 GS) is shown in **Extended Data Fig. 3a**. For spheres with embedding angle $\theta \leq \pi/2$, the friction and suction play major roles. The payload force F_p equals to the maximum resultant force of the friction and suction in the vertical direction, and can be formulated as $F_p = F_s + F_f$, where the suction force is expressed as:

$$F_s = \pi R^2 \sigma^* (\mu \sin\theta - \cos\theta)\sin^3\theta$$

The friction force is expressed as:

$$F_f = 2\pi R^2 \sigma^* (\mu \sin\theta - \cos\theta)\sin^2\theta$$

where R denotes the diameter of the sphere, and μ denotes the static friction coefficient at the gripper-sphere contact area. The above theory implying that the payload force is nearly zero when the embedding angle blew a critical embedding angle $arc\tan 1/\mu$. The payload characterization experiment also confirmed that the payload force is very limited (~10 gf) when the embedding angle is less than $60°$. For spheres with embedding angle $\theta \geq \pi/2$, the FLM and the wrapped sphere is geometrically interlocked. Furthermore, when $\theta - \pi/2 \gg 1$, only minimum interlocking occurs

(**Supplementary Fig. 5a (ii)**). The payload force F_p mainly contributed to the bend force for the wrapped sphere to slip out, and is expressed as:

$$F_p \approx (\pi/2)ER^2(t/l)^3$$

where E is the equivalent elastic modulus of FLM, and l is the thickness of the FLM wrapped around the sphere, and t is the bending arm length. When $\theta \gg \pi/2$, there is a high level of interlocking. The payload force F_p depends on the shear yield stress of the FLM σ_f, and can be formulated as:

$$F_p \approx (2\pi Rt^2/l)\sigma_f$$

We can see that the payload force increases significantly (~30 gf to ~120 gf) with the increase in the embedding angle from $90°$ to $180°$. The payload force of LiMU gripper in the interlock state far exceeds that when no interlock occurs. As concluded, the geometrically interlocked of the FLM to the surface features of the target object dominates the payload capacity of the LiMU gripper.

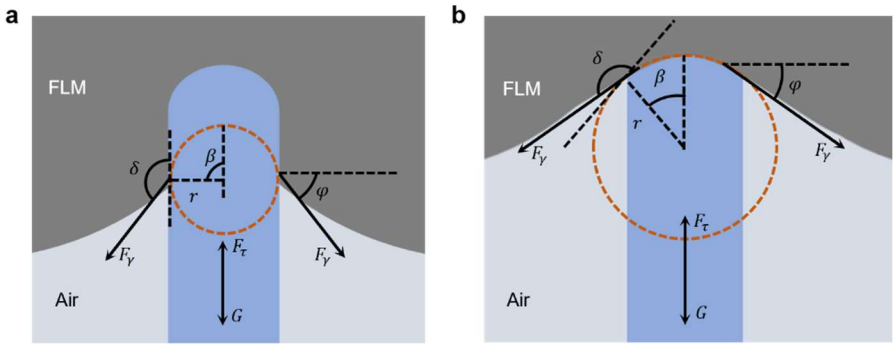

Supplementary Figure 6. (a) Dynamics of the micro-object release when the feather is immersed deeper in the FLM droplet. (b) Dynamics as the feather road is ejected from the surface of the FLM droplet.

When applying an electric field for active releasing, the force induced by the surface tension of the FLM, denoted by $F_\gamma = \gamma_s l_i$, undergoes a significant increase as the increasing of the surface tension coefficient γ_s of FLM, where l_i denotes the intersection line where the feather rod, FLM, and air meet. As shown in **Supplementary Fig. 6**, the surface tension generates a launch force F_l , that acts on the road of the immersed feather in a vertical direction,

$$F_l = F_\gamma \sin \varphi$$

where $\varphi = \delta + \beta - 180°$ denotes the tilt angle between the launch force and the horizontal direction; β represents the immersion angle and is related to the depth at which the feather rod is immersed in the FLM; $\delta = \sim 145°$ is the contact angle between the FLM and the feather rod. The dynamic changes on the surface of the FLM caused by the feather launch can be ignored. The gravity and buoyancy can be ignored for the small and lightweight target object. Thus, the dynamics of the object during the active release can be formulated as:

$$F_l - F_\tau = ma$$

where $F_\tau = \mu_v V_f$ formulates the viscous drag forces of the feather, μ_v denotes the combined viscous

coefficient of the air and FLM; V_f denotes the velocity of the feather; a and m denote the acceleration and the mass of the feather respectively.

The feather experiences two phases when launched out of the FLM droplet. When the feather is immersed deeper in the FLM droplet (**Supplementary Fig. 6a**), both the immersion angle β and the tilt angle φ remain constant and the launch force F_l acts on the road of the feather is maximum. As the the feather road is ejected from the FLM droplet surface (**Supplementary Fig. 6b**), the launch force F_l decrease to 0 with the decrease of the immersion angle β until the feather is completely separate from the FLM droplet.

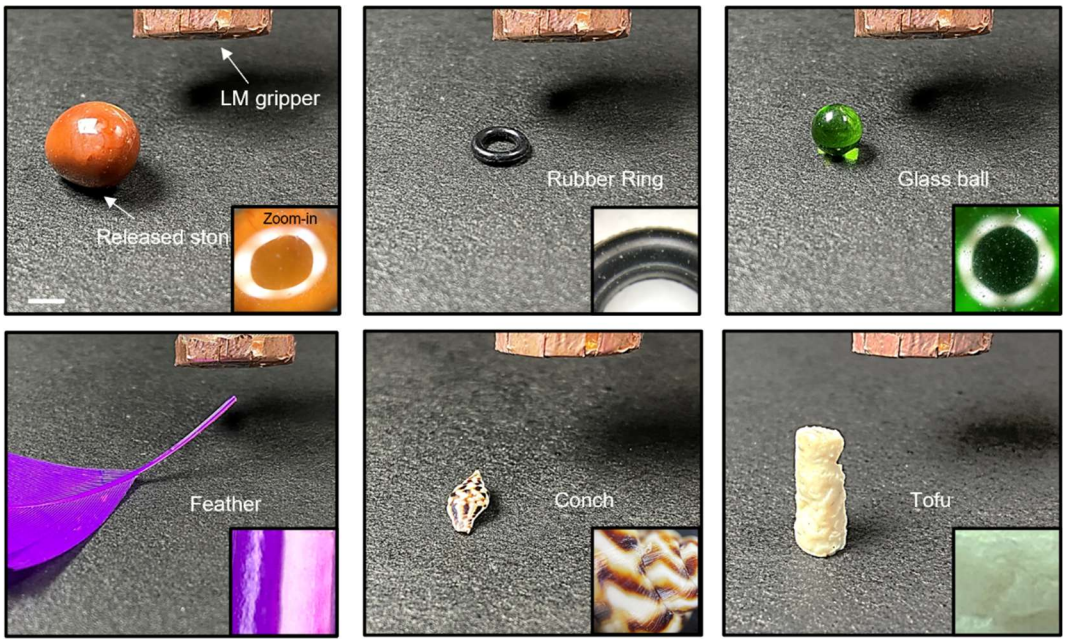

Supplementary Figure 7. Zoom-in figures show that no significant residues were found on the surfaces of released objects. Scale bar: 4 mm.

Supplementary Table 1. Acceleration of known mechanical and biological behaviors on Earth.

Category	Body length (m)	Acceleration (m/s^2)	Reference
Flea	2.0×10^{-3}	1.0×10^{1}	(*2*)
Frog	1.0×10^{-1}	1.1×10^{2}	(*3*)
BGSS	6.0×10^{-3}	1.5×10^{2}	(*4*)
Locust	5.0×10^{-2}	1.8×10^{2}	(*5*)
Spider	5.0×10^{-3}	3.7×10^{2}	(*6*)
Hummingbird	1.0×10^{-2}	2.7×10^{1}	(*7*)
Cheetah	1.2×10^{0}	1.0×10^{1}	(*8*)
Water strider-inspired robot	5.0×10^{-2}	1.4×10^{2}	(*9*)
High-speed fingered hand	1.1×10^{-1}	2.0×10^{2}	(*10*)
Rocket	3.0×10^{1}	3.0×10^{1}	(*11*)

Supplementary Table 2. The contact pressure of existing grippers and organisms.

Category	Gripper size (mm)	Contact pressure (Pa)	Reference
Jellyfish	~1.5×10^2	~1.0×10^3	(*12*)
C. elegans	~1×10^0	~1.0×10^3	(*13*)
A Multi-Material Self-Healing Soft Gripper	~1.0×10^2	~4.0×10^3	(*14*)
Electroactive polymer actuator	~4.0×10^2	~6.0×10^2	(*15*)
Kirigami gripper	~3.0×10^1	~3.8×10^3	(*16*)
Adhesive gripper	~1.0×10^2	2.5~5.0×10^3	(*17*)
Fluidic elastomer actuator (FEA) actuator	~2×10^0	~2.0×10^2	(*18*)
Soft robotic gripper for delicate structure	~1.5×10^1	~$4.5 \pm 0.7 \times 10^1$	(*12*)
Self-healing soft pneumatic gripper	~1.0×10^2	~1.5×10^2	(*19*)
Three-Fingered Soft Robotic Gripper	~1.0×10^2	~$0.5 \sim 3 \times 10^4$	(*20*)

Supplementary Reference

1 de Vicente, J., Klingenberg, D. J. & Hidalgo-Alvarez, R. Magnetorheological fluids: a review. *Soft Matter* **7**, 3701-3710 (2011).

2 Bennet-Clark, H. C. & Lucey, E. C. A. The Jump of the Flea: A Study of the Energetics and a Model of the Mechanism. *J. Exp. Biol.* **47**, 59-76 (1967).

3 James, Rob S. & Wilson, Robbie S. Explosive Jumping: Extreme Morphological and Physiological Specializations of Australian Rocket Frogs (Litoria nasuta). *Physiol. Biochem. Zool.* **81**, 176-185 (2008).

4 Challita, E. J., Sehgal, P., Krugner, R. & Bhamla, M. S. Droplet superpropulsion in an energetically constrained insect. *Nat. Commun.* **14**, 860 (2023).

5 Bennet-Clark, H. C. The energetics of the jump of the locust Schistocerca gregaria. *J. Exp. Biol.* **63**, 53-83 (1975).

6 Han, S. I., Astley, H. C., Maksuta, D. D. & Blackledge, T. A. External power amplification drives prey capture in a spider web. *Proc. Natl. Acad. Sci. U. S. A.* **116**, 12060-12065 (2019).

7 Tobalske, B. W., Altshuler, D. L. & Powers, D. R. Take-off mechanics in hummingbirds (Trochilidae). *J. Exp. Biol.* **207**, 1345-1352 (2004).

8 Wilson, A. M. *et al.* Locomotion dynamics of hunting in wild cheetahs. *Nature* **498**, 185-189 (2013).

9 Koh, J.-S. *et al.* Jumping on water: Surface tension–dominated jumping of water striders and robotic insects. *Science* **349**, 517-521 (2015).

10 Namiki, A., Imai, Y., Ishikawa, M. & Kaneko, M. in *Proceedings 2003 IEEE/RSJ International Conference on Intelligent Robots and Systems (IROS 2003) (Cat. No.03CH37453)*. 2666-2671 vol.2663.

11 Ma, L., Wang, K., Shao, Z., Song, Z. & Biegler, L. T. Direct trajectory optimization framework for vertical takeoff and vertical landing reusable rockets: case study of two-stage rockets. *Eng.*

Optimiz. **51**, 627-645 (2019).

12 Sinatra, N. R. *et al.* Ultragentle manipulation of delicate structures using a soft robotic gripper. *Sci. Rob.* **4**, eaax5425 (2019).

13 Ghanbari, A. *et al.* A micropillar-based on-chip system for continuous force measurement of C. elegans. *J. Micromech. Microeng* **22**, 095009 (2012).

14 Roels, E., Terryn, S., Brancart, J., Assche, G. V. & Vanderborght, B. in *2019 2nd IEEE International Conference on Soft Robotics (RoboSoft).* 316-321.

15 Shintake, J., Schubert, B., Rosset, S., Shea, H. & Floreano, D. in *2015 IEEE/RSJ International Conference on Intelligent Robots and Systems (IROS).* 1097-1102.

16 Yang, Y., Vella, K. & Holmes, D. P. Grasping with kirigami shells. *Sci. Rob.* **6**, eabd6426 (2021).

17 Ruotolo, W., Brouwer, D. & Cutkosky, M. R. From grasping to manipulation with gecko-inspired adhesives on a multifinger gripper. *Sci. Rob.* **6**, eabi9773 (2021).

18 Paek, J., Cho, I. & Kim, J. Microrobotic tentacles with spiral bending capability based on shape-engineered elastomeric microtubes. *Sci. Rep.* **5**, 10768 (2015).

19 Terryn, S., Brancart, J., Lefeber, D., Van Assche, G. & Vanderborght, B. Self-healing soft pneumatic robots. *Sci. Rob.* **2**, eaan4268 (2017).

20 Ariyanto, M., Munadi, M., Setiawan, J. D., Mulyanto, D. & Nugroho, T. Three-Fingered Soft Robotic Gripper Based on Pneumatic Network Actuator. *2019 6th International Conference on Information Technology, Computer and Electrical Engineering (ICITACEE)*, 1-5 (2019).